AIAA JOURNAL
Vol. 47, No. 6, June 2009

Equation of State for Energetic Structural Materials

D. Reding* and S. Hanagud†
Georgia Institute of Technology, Atlanta, Georgia 30332-0150

DOI: 10.2514/1.34472

Current investigations of energetic structural materials involve shock-induced and shock-assisted chemical reactions in which complex physical processes are currently only elucidated by computational models of gas-gun experiments. The equation of state is one of the most important parts of the constitutive models incorporated into models that describe the processes in shock-induced and shock-assisted chemical reactions. Implementation of current methods typically requires simplifying assumptions in the mixture rules. In this paper, two new equation-of-state methods are proposed that 1) are used to physically interpret both homobaric and uniform-strain assumptions, 2) do not require mixture-averaged equation-of-state model parameters, and 3) do not have any restrictions on the form of constituent equation-of-state or pore-collapse model. The proposed methods are compared with other mixture equation-of-state methods, and cases in which the mixture is porous are demonstrated. Gas-gun experiments are simulated and compared with experimental data for a material with 2Al, Fe_2O_3, 20 wt % Epon 828, and voids, in which the reaction initiation threshold was not reached. The simulation integrates conservation equations and momentum balance using a second-order finite volume scheme.

Nomenclature

A	=	frequency factor
C	=	acoustic velocity
C_m	=	fraction of the pressure from the homobaric-mixture assumption
C_p	=	specific heat capacity at constant pressure
C_v	=	specific heat capacity at constant volume
E	=	total energy
e	=	specific internal energy
k_q	=	heat conduction coefficient
M	=	molar mass
n	=	distension-ratio pressure dependency
P	=	pressure
P^e	=	pore elastic-yield strength
P^s	=	pore crush strength
$\boldsymbol{q}$	=	heat flux vector
S_1	=	slope of the linear U_s–U_p curve
T	=	temperature
T_m	=	melting temperature
t	=	time
U_p	=	particle velocity
U_s	=	shock velocity
v	=	specific volume
$\mathbf{v}$	=	velocity vector
Y	=	initial yield stress
α	=	porosity or distension ratio
β_{x_o}	=	bulk modulus at the reference temperature
β'_{x_o}	=	pressure derivative of β_{x_o}
Γ	=	Grüneisen parameter
ΔH_m	=	latent heat of melting
$\boldsymbol{\epsilon}$	=	strain tensor
Θ	=	reaction rate
λ	=	maximum eigenvalue
μ	=	shear modulus
μ_c	=	specific chemical potential
ν	=	stoichiometric coefficient
ξ	=	volume fraction
ρ	=	density
$\boldsymbol{\sigma}$	=	stress tensor
ϕ	=	mass fraction

Presented as Paper 2034 at the 48th AIAA/ASME/ASCE/AHS/ASC Structures, Structural Dynamics, and Materials Conference, Honolulu, HI, 23–26 April 2007; received 5 October 2007; revision received 28 February 2008; accepted for publication 25 August 2008.

*Graduate Research Assistant, School of Aerospace Engineering. Student Member AIAA.

†Professor, School of Aerospace Engineering. Fellow AIAA.

I. Introduction

ENERGETIC structural materials (ESMs) are a new class of materials that provide dual functions of strength and energetic characteristics. These materials are typically composed of micron-scale or nanoscale intermetallic particles such as Ni and Al and mixtures of metals and metal oxides such as 2Al and Fe_2O_3. Structural reinforcements, polymer binder, and voids are included to produce a composite with relatively low density and improved material strength characteristics compared with conventional explosives. ESMs can have similar energy release compared with conventional explosives, however, reaction may not yield gas products. Gasless ESM reactions are called heat detonations [1]. The material failure criteria for ESMs must include the following two failure modes:

1) In strength-based modes of failure, the material must not fail due to lack of sufficient strength when impacted or when exposed to high temperature.

2) In reaction-based failure, reaction results are due to encountered impact or high temperature during operation.

Designing ESMs is difficult because chemical reaction and plastic flow in these complex materials is not currently well understood. These physical processes cannot be directly observed with current technology. Gas-gun or explosive loading experiments have been the only experiments used to study ESMs and similar metallic powder mixtures under shock conditions [2–4]. These experiments are also known as Hugoniot experiments, in which pressure and shock velocity data are obtained (e.g., see Thadhani et al. [5]). Simulations of ESMs with shock loading have been performed [6–10] and, in a few cases, chemical reactions have been included [6,7].

Because the physical processes involved in shock compression of ESMs are coupled, we are forced to rely solely on Hugoniot experiments to obtain multiple material constants in existing models [1,6,7,11–18]. These models have greatly improved our understanding of experimental results involving postshock examination and real-time measurements. Two main classes of models proposed to explain shock-induced chemical reactions (SICRs) and shock-assisted chemical reactions (SACRs) are continuum-level modeling [1,7,8,15] and spatially resolved particle systems or discrete particle

simulation (DPS) [8,19]. SICRs are initiated within time scales of mechanical (pressure) equilibration. SACRs are initiated on larger time scales of thermal equilibration (i.e., after release waves have allowed mechanical relaxation [20]).

In this paper, we are motivated to find accurate and physically meaningful methods to predict the equation of state (EOS) in porous mixtures. The propagation of a shock wave in a mixture depends almost entirely on the EOS. Therefore, small differences between various mixture EOS models can result in large differences in simulated shock velocity. During shock compression of ESMs, chemical reaction and pore collapse produce greatly increased temperatures with relatively low pressures. Existing EOS methods [1,15,16,21,22] employ averages of constituent EOS parameters, losing physically meaningful information. Accurate and physically meaningful EOS predictions are critical for predicting the influence of chemical reactions on shock velocity.

Several continuum models have been introduced to describe pore collapse in energetic granular metallic mixtures during intense dynamic loading [1,6,7,14–16,18,23]. All of these models employ the widely used P–α model by Herrmann [24] to describe pore collapse. A quadratic dependence of porosity on pressure is assumed for all of these studies except for one, in which a linear dependence is used [23]. The P–α model is an equation of state, and thus time-dependent effects due to inertia, plastic hardening, and strain-rate dependencies cannot be included. An alternative to the P–α model is the single-pore model with spherical symmetry, which includes viscoplasticity and dynamic effects for a single constituent. Examples include the Carroll–Holt model [25,26] with a hollow-sphere geometry and the modified Carroll–Holt model by Nesterenko [27] with a nondeformable central core. A critical analysis of spherically symmetric models is given by Nesterenko [28].

DPS models have increased physical modeling capabilities compared with continuum approaches. In contrast to the continuum approach, DPS models capture plastic flow phenomenon, mixing behavior, and pore collapse without using a porous-mixture model. The DPS approach requires an EOS model for each constituent in the mixture [19], which includes products formed by reaction or mixing of two or more constituents. Molecular dynamics (MD) approaches offer increased accuracy compared with DPS models. However, MD models are restricted to much smaller length and time scales.

Although DPS and MD models offer significant advantages, we are motivated to pursue the formulation of continuum-level EOS models for two reasons. First, DPS and MD studies are restricted to much smaller length and time scales compared with continuum-level models (with current computing limitations). Second, continuum-level models are required in large-scale applications in which the mesh size is far greater than the dimension of the mixture particles.

Our focus is to formulate two new continuum-level porous-mixture EOS models and to compare them with three alternative methods [1,15,16,21,22]. We implement the proposed methods in a code written by the authors in which the conservation equations and momentum balance are solved in Eulerian coordinates using a second-order finite volume method. A case study is used to demonstrate the proposed methods for mixtures containing Al, Fe_2O_3, Epon 828, and voids. Shock experiments for this type of ESM have not shown evidence of chemical reaction and are therefore not addressed in this paper.

II. Continuum Model

This section provides fundamental equations and relationships used in the ESM continuum model. Assumptions for the mixture rules are followed by the conservation laws.

A. Mixture Rules

Mixture quantities are approximated by use of mixture averages of constituents with separate phases p based on volume fractions ξ_p, surface-area fractions ς_p, and mass fractions ϕ_p in the fully dense, or nonporous, portion of the mixture. The surface-area fraction ς corresponds to partial traction and partial stress description, discussed in more detail in Sec. III.A. Each constituent is permitted to evolve independently with time. Each of these quantities sums to unity: that is,

$$\sum_p \xi_p = 1; \qquad \sum_p \varsigma_p = 1; \qquad \sum_p \phi_p = 1 \tag{1}$$

The overbar for all quantities indicates an averaged mixture quantity, unless otherwise specified. There are three mixture-averaged quantities.

The volume-averaged quantity is density:

$$\bar{\rho}^{\,d} = \sum_p \xi_p \rho_p \tag{2}$$

Summing over all the constituents on the right-hand side of Eq. (2) is equivalent to summing the partial masses divided by the entire volume occupied by the mixture. By dividing Eq. (2) by $\bar{\rho}^d$, the mass fraction is defined by

$$\phi_p = \xi_p \frac{\rho_p}{\bar{\rho}^d} \tag{3}$$

The nonporous-mixture density is written in terms of the mass fraction by

$$\frac{1}{\bar{\rho}^d} = \frac{\phi_p}{\rho_p \xi_p} = \sum_p \frac{\phi_p}{\rho_p} \tag{4}$$

The porous-mixture density $\bar{\rho}$ is defined in Eq. (31).

The surface-averaged quantities are heat flux, surface traction vector, and Cauchy stress tensor:

$$\bar{\boldsymbol{q}} = \sum_p \varsigma_p \boldsymbol{q}_p; \qquad \bar{\boldsymbol{t}} = \sum_p \varsigma_p \boldsymbol{t}_p; \qquad \bar{\boldsymbol{\sigma}} = \sum_p \varsigma_p \boldsymbol{\sigma}_p \tag{5}$$

where $\bar{\boldsymbol{q}}$ is analogous to the mixture strength discussed in Sec. III.A.

The mass-averaged quantities are velocity vector, specific internal energy, and specific heat:

$$\bar{\mathbf{v}} = \sum_p \phi_p \mathbf{v}_p; \qquad \bar{e} = \sum_p \phi_p e_p; \qquad \bar{C}_v = \sum_p \phi_p C_{vp} \tag{6}$$

B. Conservation Laws

Conservation of mass, momentum, and energy are the governing equations for hydrodynamic simulations involving the passage of shock waves. Equations (7–38) are for the continuum model (macroscale) in which mixture averages are used. The following equations do not include mass diffusion (i.e., $\mathbf{v}_p = \bar{\mathbf{v}}$ for all constituents p). The conservation equations and momentum balance are given by the following three equations, written in spatial (Eulerian) coordinates:

$$\frac{\partial}{\partial t}(\bar{\rho}) + \nabla \cdot (\bar{\rho}\,\bar{\mathbf{v}}) = 0 \tag{7}$$

$$\frac{\partial}{\partial t}(\bar{\rho}\,\bar{\mathbf{v}}) + \nabla \cdot (\bar{\rho}\,\bar{\mathbf{v}} \times \bar{\mathbf{v}}) = \nabla \cdot \bar{\boldsymbol{\sigma}} + \bar{\rho}\,\bar{\boldsymbol{f}} + \bar{\boldsymbol{\Psi}}_m \tag{8}$$

$$\frac{\partial}{\partial t}(\bar{E}) + \nabla \cdot (\bar{E}\,\bar{\mathbf{v}}) = \nabla \cdot (\bar{\boldsymbol{q}}) + \bar{\boldsymbol{\sigma}} : \dot{\bar{\boldsymbol{\epsilon}}} + \bar{\Psi}_e \tag{9}$$

where t is the time, $\bar{\boldsymbol{f}}$ is the specific body force vector, $\bar{\boldsymbol{\sigma}}$ is the stress tensor that is defined later in this section, $\dot{\bar{\boldsymbol{\epsilon}}}$ is the strain-rate tensor (rate of deformation tensor), the source terms $\bar{\boldsymbol{\Psi}}_m$ and $\bar{\Psi}_e$ are defined subsequently, and $\bar{E}$ is the total energy in the mixture and is defined as

$$\bar{E} = \bar{\rho}^d (\bar{e} + \tfrac{1}{2}\bar{\mathbf{v}} \cdot \bar{\mathbf{v}}) \tag{10}$$

where $\bar{e}$ is the specific internal energy in the dense mixture, because the surface energy of the pores is neglected (see Sec. III.B.2) and is defined as

$$\bar{e} = \bar{C}_v \bar{T} \tag{11}$$

where $\bar{C}_v$ is the mass-fraction-averaged specific heat capacity at constant pressure in the dense mixture. Equation (7) is supplemented by $(n_p - 1)$-independent constituent equations (where n_p is the total number of constituents in the mixture), given by

$$\frac{\partial}{\partial t}(\phi_p \bar{\rho}) + \nabla \cdot (\phi_p \bar{\rho} \bar{\mathbf{v}}) = \Psi_{\text{mass } p} \tag{12}$$

The rate of mass production is

$$\Psi_{\text{mass } p} = \Theta M_p v_p \tag{13}$$

where Θ is the phase transformation rate, M_p is the molar mass, and v_p is the stoichiometric coefficient for constituent p. The source terms $\bar{\boldsymbol{\Psi}}_m$ and Ψ_e are due to the phase changes in Eq. (12) and only apply to the continuum-level model. $\bar{\boldsymbol{\Psi}}_m$ in Eq. (8) represents the change in momentum due to phase changes and is composed of linear and angular momentum contributions, respectively:

$$\bar{\boldsymbol{\Psi}}_m = \sum_p \Psi_{\text{mass } p}(\mathbf{v}_p + \mathbf{x}_p \times \mathbf{v}_p) \tag{14}$$

where $\mathbf{x}_p$ is the material coordinate for the pth constituent. The source term Ψ_e in Eq. (9) represents the energy contribution due to phase changes and is given by

$$\bar{\Psi}_e = \sum_p \Psi_{\text{mass } p}\left(\frac{1}{2}\mathbf{v}_p \cdot \mathbf{v}_p + \mu_{cp}\right) \tag{15}$$

where μ_{cp} is the specific chemical potential for the pth constituent. The latent heat of melting ΔH_{mp} is accounted for in the numerical solution by limiting the temperature at the melting temperature T_{mp} for constituent p until melting is complete. The corresponding difference in the internal energy $\bar{e}$ is used to calculate the amount of melting at each time step.

III. Constitutive Relationships

A. Mixture Strength

Mixture strength is required in a continuum description of the granular mixture before and after the pores have collapsed. In the macroscale, each constituent in the mixture is separated by interfaces with other constituents. Physical discreteness is transformed to a mathematical continuum. Therefore, interactions that occur on the interface between constituents must be treated as internal actions in each constituent continua [29].

We follow the partial traction and partial stress description by Rajagopal and Tao [29], in which $\mathcal{S}$ is a surface in the body, and $\mathbf{n}_{\mathcal{S}}$ is the normal vector to $\mathcal{S}$ at the point $\mathbf{x}$ contained within the body. The notation presented here is altered from the form given by Rajagopal and Tao by defining the traction vector $\boldsymbol{t}_p$ and the Cauchy stress tensor $\boldsymbol{\sigma}_p$ associated with each constituent p in the mixture, where

$$\boldsymbol{t}_p = (\boldsymbol{\sigma}_p)^T \mathbf{n}_{\mathcal{S}} \tag{16}$$

Because this paper is focused on small-particle mixtures such as micron-scale or nanoscale intermetallic particles, we assume that the probability of the mixture constituent p in contact with $\mathcal{S}$ is equal to its occupied volume fraction: that is,

$$\varsigma = \xi_p \tag{17}$$

The physical basis for this assumption comes from reducing the size of particles with uniform geometry. This assumption is invalid for mixtures containing particles with different geometry (e.g., flake and spherical particles).

Using the assumption in Eq. (17), the total mixture traction $\bar{\boldsymbol{t}}$ and Cauchy stress tensor $\bar{\boldsymbol{\sigma}}$ are given by

$$\bar{\boldsymbol{t}} = \sum_p \xi_p \boldsymbol{t}_p \tag{18}$$

and

$$\bar{\boldsymbol{\sigma}} = \sum_p \xi_p \boldsymbol{\sigma}_p \tag{19}$$

so that

$$\bar{\boldsymbol{t}} = \bar{\boldsymbol{\sigma}}^T \mathbf{n}_{\mathcal{S}} \tag{20}$$

The Cauchy stress tensor in Eq. (19) is decomposed into its hydrostatic P and deviatoric $\boldsymbol{\sigma}'$ components:

$$\bar{\boldsymbol{\sigma}} = -\bar{P}\boldsymbol{I} + \bar{\boldsymbol{\sigma}}' \tag{21}$$

where $\boldsymbol{I}$ is the second-order identity tensor. Thermomechanical constitutive relationships include an equation of state in the form $P_p = f_p(\rho, e)$ and a strength relationship in the form $\boldsymbol{\sigma}'_p = \boldsymbol{\sigma}'_p(\boldsymbol{D}, \bar{T}, \boldsymbol{z})$, where $\boldsymbol{D}$ is the deformation rate, $\bar{T}$ is the mixture temperature, and $\boldsymbol{z}$ are internal state variables.

Thermodynamic equilibrium is assumed between mixture constituents only in the macroscale model. The nonequilibrium case is discussed later. According to the thermodynamic equilibrium assumption and using Eq. (17), the mixture average shear modulus is written as

$$\bar{\mu}(\bar{T}) = \frac{1}{\alpha_o}\sum_p \xi_p \mu_p(\bar{T}) \tag{22}$$

where $\mu_p(\bar{T})$ is assumed to depend linearly on temperature such that $\mu_p(\bar{T} = T_o) = \mu_o$ and $\mu_p(\bar{T} = T_{m,p}) = 0$, T_m is the melting temperature, $\bar{\mu}(\bar{T}) = 0$ when $T \geq T_{m,p}$ for any constituent p in the mixture, α_o is the porosity defined in Eq. (30), and the subscript o denotes the initial or zero-pressure state.

We assume the material yields when the equivalent stress exceeds the mixture yield stress (i.e., $\sigma_{\text{eq}} > \bar{Y}_{\text{mix}}$). Von Mises or maximum-distortion-energy criteria are used, and the radial return method is applied to the stress deviators. For gas-gun simulations, we assume one-dimensional strain, which is often a good approximation [22]; equivalent stress is given by

$$\sigma_{\text{eq}} = \sqrt{\tfrac{3}{2}((\bar{\sigma}'_{xx})^2 + 2(\bar{\sigma}'_{yy})^2)} \tag{23}$$

where the shock propagates along the x axis. The deviators are given in rate form by

$$\dot{\bar{\sigma}}'_{xx} = \frac{4}{3}\bar{\mu}\frac{\partial \bar{\mathrm{v}}_x}{\partial x}; \qquad \dot{\bar{\sigma}}'_{yy} = \dot{\bar{\sigma}}_{zz} = -\frac{2}{3}\bar{\mu}\frac{\partial \bar{\mathrm{v}}_x}{\partial x} \tag{24}$$

Equation (24) is valid for small strains and is appropriate for mixtures containing binders such as epoxy, because these materials yield at small strains.

The porous-mixture yield strength is given by

$$\bar{Y}_{\text{mix}} = \frac{1}{\alpha}\bar{Y} \tag{25}$$

where the assumption in Eq. (17) gives us

$$\bar{Y} = \sum_p \xi_p Y_p \tag{26}$$

Constituent yield strength Y_p generally depends on the effective mixture shear strain rate $\dot{\bar{\gamma}}$ and mass-fraction-averaged temperature $\bar{T}$ [i.e., $Y_p = Y_p(\dot{\bar{\gamma}}, \bar{T})$]. However, in this paper, our focus is on the pressure-density relationship; therefore, we assume that Y_p has a constant value.

B. Pressure-Density Relationship

1. *Single-Constituent Equation of State*

Two models used for the high-pressure regimes found in shock physics are the Mie–Grüneisen (as discussed in [30]) and Murnaghan [31] EOS models. Much of the experimental EOS data collected for solids and liquids have been fit to these models.

The Mie–Grüneisen EOS is extensively used in the determination of shock and residual temperatures and for predicting the shock response of porous materials [22]. The Mie–Grüneisen EOS can easily be derived from the Rankine–Hugoniot equations [22] and is written in terms of the specific energy e or temperature T and specific volume $v = 1/\rho$ as

$$P(e, v) = \frac{C_o^2(v_o - v)}{[v_o - S_1(v_o - v)]^2} + \frac{\Gamma}{v}\left[e - \frac{1}{2}\left(\frac{C_o(v_o - v)}{v_o - S_1(v_o - v)}\right)^2\right] \tag{27}$$

where C_o is the acoustic wave speed, S_1 is the slope of the linear U_s–U_p curve (U_s is the shock velocity), U_p is the particle velocity, and Γ is the Grüneisen parameter. Equation (27) is not easily inverted [i.e., solved for $\rho(P)$].

The Grüneisen parameter is defined as

$$\Gamma = V\left(\frac{\partial P}{\partial e}\right)_V = \frac{\Gamma_o \rho_o}{\rho} \tag{28}$$

The Murnaghan EOS is derived from the variation of bulk modulus with respect to pressure and takes the form in terms of reference temperature T_o as

$$P = \frac{\beta_{T_o}}{\beta'_{T_o}}\left[\left(\frac{\rho}{\rho_o}\right)^{\beta'_{T_o}} - 1\right] + C_v \Gamma \rho_o (T - T_o) \tag{29}$$

where $\beta_{T_o} = -V(\partial P/\partial V)|_{T_o}$ is the isothermal bulk modulus at the reference temperature, $\beta'_{T_o} = (\partial \beta/\partial P)|_{T_o}$ is the pressure derivative of the isothermal bulk modulus at the reference temperature, C_v is the specific heat capacity at constant volume, and ρ_o is the reference density.

2. *Single-Constituent Pore-Collapse Equation of State*

The P–α model by Herrmann [24] in Eq. (30) is a pore-collapse EOS that has been successfully applied [15,25] assuming a quadratic dependence on pressure [i.e., $n = 2$ in Eq. (30)]. The porosity α, defined in terms of density in Eq. (31), is simplified in this paper from the general form $\alpha = g(P, e)$:

$$\alpha = \begin{cases} \alpha_o; & P < P^e \\ 1 + (\alpha_o - 1)[(P^s - P)/(P^s - P^e)]^n; & P^e \le P \le P^s \\ 1; & P^s < P \end{cases} \tag{30}$$

where he parameter n describes the order of porosity dependence on the pressure P and is left as a general unknown material parameter, and P^e and P^s are the elastic threshold and pore-collapse strength, respectively. For $P < P^e$, only elastic deformation is assumed to take place, and for $P > P^s$, complete closure of the voids is assumed. The porosity is a measure of the void content and is expressed in terms of specific volume v and density ρ by

$$\alpha = \frac{v}{v_d} = \frac{\rho^d}{\rho} \ge 1 \tag{31}$$

where the densities ρ^d and ρ correspond to the dense and porous material at the same temperature and pressure.

The central assumption used in the P–α model is that specific internal energy is the same for the porous material and the fully dense material under identical conditions of pressure and temperature [24]. This assumption implies that the surface energy of the pores is neglected. The equation of state for the porous material is denoted by

$$P = f(v_d, e) = f\left(\frac{v}{\alpha}, e\right) \tag{32}$$

3. *Porous-Mixture Equation of State*

Two possible limiting mixture assumptions with physical interpretation are the homobaric and uniform-strain assumptions. The schematic shown in Fig. 1 illustrates these assumptions for a one-dimensional (1-D) strain case for a mixture with four constituents and voids that are consistent with the P–α model. The use of the assumption in Eq. (17) and the P–α model implies that voids do not carry any of the load. If we let σ_{xx} be the total stress applied to the mixture with area dA in 1-D strain, then the stress applied to the solid mixture in Fig. 1 is given by assumption (17) as

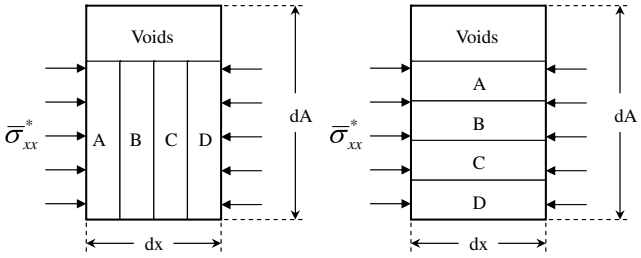

a) Homobaric mixture **b) Uniform strain**

Fig. 1 Limiting-case porous-mixture theories.

$$\frac{1}{\alpha}\bar{\sigma}^*_{xx} = \bar{\sigma}_{xx} \tag{33}$$

The uniform-strain assumption states that the strain is equal for all constituents, as shown in Fig. 1b, and thus constituent volume fractions remain constant. The uniform-strain assumption may be viewed as an idealization of an infinitely thin slice of the mixture material or as $\Delta x \to 0$ in Fig. 1b. This assumption states that mechanical equilibrium has not been reached. In this case, we assume from Eq. (17) that the surface area of each constituent is proportional to its volume fraction. Therefore, the pressure for the porous mixture $\bar{P}$ is approximated by Eqs. (17–21).

In this paper, we apply the homobaric and uniform-strain assumptions without using mixture rules [1,15,16,21,22] to calculate EOS parameters. In addition, we construct the proposed methods to accept any pore-collapse model. To demonstrate the proposed porous-mixture EOS methods, we modify the P–α model by Herrmann [24] to incorporate the mixture. The form in Eq. (32) is modified to include more than one constituent. The pressure for the porous mixture $\bar{P}$ in Eqs. (35a) and (35b) includes contributions from constituents p by using the porous volume fractions: that is,

$$\alpha \sum_p \xi_p = 1 \tag{34}$$

The homobaric and uniform-strain assumptions are applied to Eq. (32) with porosity from Eq. (34) and are stated as

$$\bar{P}_{ho} = \alpha \sum_p f_p\left(\frac{\rho_{op}}{\rho_p}, \bar{T}\right)\xi_p; \qquad P_p = P_r \quad \text{for } p \ne r \tag{35a}$$

$$\bar{P}_{us} = \alpha \sum_p f_p\left(\frac{\bar{\rho}^d_o}{\bar{\rho}^d}, \bar{T}\right)\xi_p; \qquad \frac{\rho_p}{\rho_{op}} = \frac{\bar{\rho}^d}{\bar{\rho}^d_o} \quad \text{for all } p \tag{35b}$$

Components in the mixture are in thermal equilibrium and satisfy the assumption that specific internal energy is the same for porous material and fully dense material. The form f_p is the pressure EOS for each solid- or liquid-mixture constituent p. The porous-mixture average density $\bar{\rho}$ with porosity α has the corresponding initial values $\bar{\rho}_o$ and α_o at $t = 0$, and so the dense mixture has the average density $\bar{\rho}^d_o = \bar{\rho}\alpha_o$.

The assumption of thermal equilibrium (i.e., $T_p = \bar{T}$ for all constituents p) may be relaxed if the last two expressions in Eq. (6) are employed. This approach may be used for mixtures containing particles larger than micron scale or nanoscale. The nonequilibrium temperature extension to the model in Eqs. (35a) and (35b) is completed by the heat transport equation (38).

Equations (35a) and (35b) are implicit and are solved using the bisection method iteratively, as seen in the algorithms given in Fig. 2.

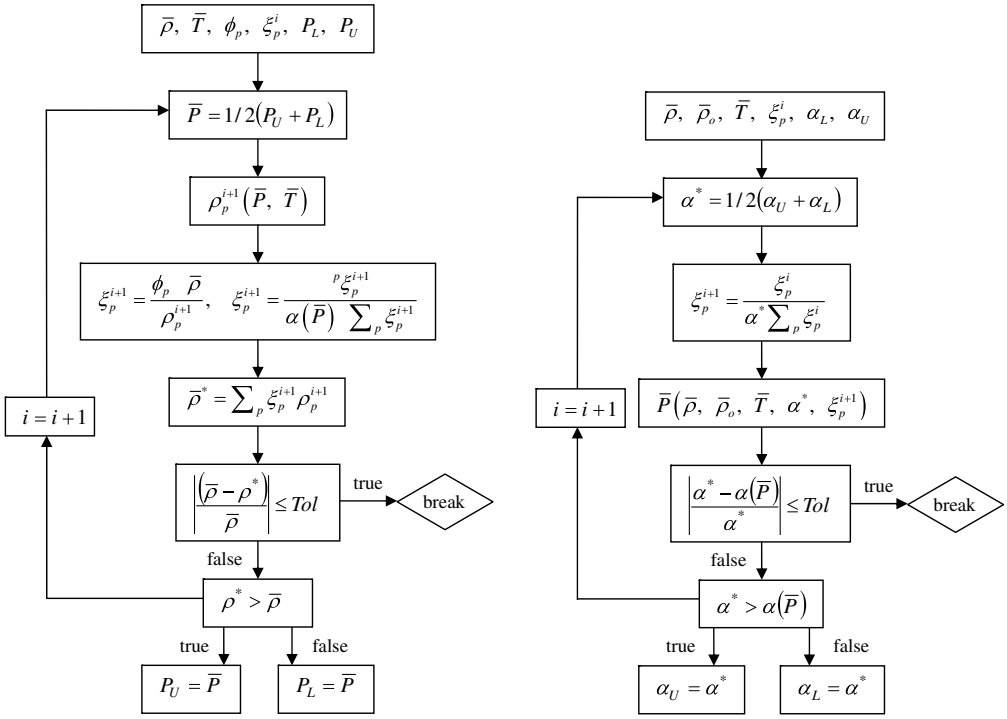

a) Homobaric mixture **b) Uniform strain**

Fig. 2 Mixture EOS algorithms.

The bisection method is chosen over potentially faster methods for robustness.

The homobaric algorithm in Fig. 2a uses the new mass fractions that remain constant during the iterations. Constituent volume fractions are recalculated until the mixture density converges.

The uniform-strain algorithm in Fig. 2b uses the initial volume fractions. When chemical reactions change the mass fractions, the reference density $\bar{\rho}_o^d$ is calculated using $\rho_p = \rho_{op}$ in Eqs. (3) and (2). From the definition of the uniform-strain assumption, shown previously, the ratio of the volume fractions between constituents remains constant. Therefore, volume fractions are proportionally scaled according to Eq. (34).

These algorithms require the supplementary relationships

$$\xi_p^{i+1} = \frac{\xi_p^{i+1}}{\alpha^{i+1}\sum_p \xi_p^{i+1}} \tag{36a}$$

$$\rho_p = f_p^{-1}(\bar{P}, \bar{T}) \tag{36b}$$

$$\rho_p = f_p^{-1}(P_p(\bar{\rho}^d, \bar{T})) \tag{36c}$$

Equation (36a) is used to normalize the new volume fractions to ensure that Eq. (34) is satisfied when pores collapse. Equations (36b) and (36c) are used to calculate the new density by inverting the EOS for each constituent using the homobaric and uniform-strain assumptions, respectively. This step is straightforward when the constituent EOS takes the Murnaghan form in Eq. (29). However, inverting the Mie–Grüneisen EOS in Eq. (27) requires an iterative scheme.

In practice, tight tolerances (0.0001% error) are used for the proposed algorithms. Although this tolerance is computationally expensive with approximately 20 iterations, high-accuracy results are obtained.

We define the mixture parameter C_m as the fraction of the pressure from homobaric-mixture assumption, $\bar{P}_{ho}$. This mixture rule is stated as

$$P_{\text{mix}} = \bar{P}_{ho} \cdot C_m + \bar{P}_{us} \cdot (1 - C_m) \qquad 0 \le C_m \le 1 \tag{37}$$

Pressure equilibration in simulated mixtures occurs well within the rise time of a shock wave [8]; therefore, we would expect that $C_m \to 1$, to approximate real mixtures.

C. Heat Conduction

Fourier's law in Eulerian coordinates for material convective transfer takes the vector form:

$$\bar{\boldsymbol{q}} = -\bar{k}_q \nabla \bar{T} + \bar{C}_v \bar{\rho}^d \bar{\mathbf{v}}\, \bar{T} \tag{38}$$

where $\bar{k}_q$ is the volume-fraction-averaged heat conduction coefficient, and $\bar{C}_v$ is the mass-fraction-averaged specific heat capacity at constant volume in the dense mixture. The assumption in Eq. (17) is employed and these quantities are calculated using the mixture rules in Eqs. (2–6).

IV. Case Study: 2Al, Fe_2O_3, Epon 828, and Voids

We consider shock compression of a mixture containing 2Al and Fe_2O_3 in stoichiometric quantities with up to 20 wt % Epon 828 and porosity as high as $\alpha = 1.666$. Initial mass fractions and corresponding volume fractions of the dense mixture ξ_o are given in Table 1.

Constituent Grüneisen and Murnaghan EOS parameters are given in Table 2 and remaining material parameters are given in Table 3. For simplicity, the Grüneisen parameter is assumed to be constant and is estimated using the common approximation $\Gamma = 2S_1 - 1$ [22]. All other Grüneisen parameters were obtained from Marsh [32], in which values for $Al_{(s)}$ were taken from the Al-1100 data. Further details are given by Austin [8]. All of the Murnaghan parameters are obtained from Bennett et al. [15], with the exception of the isothermal bulk modulus [1] β_{T_o}, because these values are reported 1 order of magnitude too low.

We need to ensure that the Mie–Grüneisen and Murnaghan EOS models produce close pressures to make fair comparisons between mixture models. The Murnaghan EOS constituent parameters for Al and Fe_2O_3 are adjusted in Table 2 to approximate the $T = 298$ K isotherm pressure calculated using the Mie–Grüneisen model.

Table 1 Input parameters used in the stoichiometric Al/Fe_2O_3–Al_2O_3/2Fe reaction

Parameter	Al	Fe_2O_3	Al_2O_3	Fe	Epon 828	Units
M	26.98	159.69	101.96	55.85	——	$g \cdot mol^{-1}$
ν	2	1	1	2	——	——
ϕ_o	0.2526	0.7474	0	0	0	——
ξ_o [a]	0.3976	0.6024	0	0	0	——
ϕ_o (20 wt % Epon 828)	0.2021	0.5979	0	0	0.20	——
ξ_o [a] (20 wt % Epon 828)	0.2109	0.3195	0	0	0.4696	——

[a]Calculated by Eq. (3) using solid densities in Table 2.

Table 2 Equation-of-state and thermodynamic material parameters

Parameter	$Al_{(s)}$	$Al_{(l)}$	$Fe_2O_{3(s)}$	$Al_2O_{3(l)}$	$Fe_{(l)}$	Epon 828	Units
ρ_o	2700	2380	5274	2960	6590	1200	$kg \cdot m^{-3}$
C_p	0.90	0.90 [a]	0.607	0.714	0.450	2.10	$kJ \cdot kg^{-1} \cdot K^{-1}$
k_q	222	222 [a]	5	35	76.2	0.2	$W \cdot m^{-1} \cdot K^{-1}$
Γ	2.00	2.00 [a]	1.99	1.32	2.10	2.18 [c]	——
C_o	5.38	——	6.30	——	——	2.60	$km \cdot s^{-1}$
S_1	1.34	——	1.176	——	——	1.59	——
β_{S_o}	76.7/79.0 [c]	52.3	202.7/207.0 [c]	252.0	136.0	8.11 [b]	GPa
β'_{S_o}	3.693	3.693 [a]	4.35	5.00	3.97	5.36 [b]	——

[a]Indicates that the solid properties were used.
[b]Grüneisen values are used with approximations from Eq. (40).
[c]Adjusted to fit the Grüneisen $T = 298$ K isotherm over the range $0 \le P \le 30$ GPa).

Table 3 Reactant material parameters

Parameter	Al-1100 [37]	Fe_2O_3 [a]	Epon 828 [a]	Units
Shear modulus μ_o	26.0	104	1.4	GPa
Yield strength Y	105	800	60	MPa
Melting temperature T_m	926	1780	533	K
Latent heat of melting ΔH_m	390	600	——	$kJ \cdot kg^{-1}$

[a]Estimated from Austin [8,9].

A. Equation-of-State Mixture Rules

Several methods have been employed [1,15,16,21,22] to calculate the mixture EOS by using Mie–Grüneisen and Murnaghan EOS models with mass- or volume-fraction-averaged material parameters. We compare the proposed mixture EOS methods in Fig. 2 with three existing methods.

1. Mixture Rules for Mechanical Equilibrium

This is a method that is consistent with the assumption that a mixture is in mechanical equilibrium [16], and it is employed in studies of SICRs [1,15,16]. The mixture-averaged isentropic bulk modulus and pressure derivative in this method are given, respectively, by

$$\bar{\beta}_{S_o} = \frac{1}{\bar{\rho}_o}\left[\sum_p \frac{\phi_p}{\rho_{op}\beta_{S_o p}}\right]^{-1}$$

$$\bar{\beta}'_{S_o} = \bar{\rho}_o \bar{\beta}^2_{S_o}\left[\sum_p \frac{\phi_p(1+\beta'_{S_o p})}{\rho_{o,p}\beta^2_{S_o p}}\right] - 1 \tag{39}$$

where $\bar{\rho}$ is calculated from Eq. (4). This method assumes that

$$\beta_{T_o} \cong \beta_{S_o} = \rho_o C_o^2; \qquad \beta'_T \cong \beta'_S = 4S_1 - 1 \tag{40}$$

The following relationship is assumed:

$$\rho\Gamma = \rho_o \Gamma_o \tag{41}$$

The quantities $\bar{C}_v$ and $\bar{\Gamma}$ are grouped together and approximated by the mixture rule given in the extended void-inert-reactive (VIR) model by Bennett et al. [15] in Eq. (42):

$$\bar{C}_v \bar{\Gamma} = \bar{\beta}_T \sum_p \frac{\phi_p C_{vp} \Gamma_p}{\beta_{Tp}} \tag{42}$$

.

2. Mixture Rule Based on Mass-Fraction Averages at 0 K Isotherms (Method 2)

This is the more rigorous of the two methods (developed by McQueen et al. [21]) and is widely used for alloys and compounds. Pressure is calculated by solving the differential equation:

$$\left(\frac{dP}{dv}\right)_{T_o} + \frac{\Gamma_o}{v_o} P_{T_o} = \frac{\Gamma_o}{2v_o}\left[P_H + \left(\frac{v_o}{\Gamma_o} + v - v_o\right)\left(\frac{C_o^2 + 2S_1[v_o - S_1(v_o - v)]}{[v_o - S_1(vo - v)]^4}\right)\right] \tag{43}$$

where the subscript o denotes the reference state and P_{T_o} is the pressure at the reference state temperature T_o. All terms on the right-hand side of Eq. (43) are known because

$$P_H = \frac{C_o^2(v_o - v)}{[v_o - S_1(v_o - v)]^2} \tag{44}$$

This method employs mass-fraction averages for quantities in Eq. (43). For example, the heat capacity is

$$\bar{C}_v = \sum_p \phi_p C_{vp}$$

A mass-fraction average is used to calculate the Grüneisen ratio as

$$\left(\frac{\bar{v}_o}{\bar{\Gamma}_o}\right) = \sum_p \phi_p \left(\frac{v_{op}}{\Gamma_{op}}\right) \tag{45}$$

We compute the 0 K isotherm using Yoshida's MIXTURE program [33] to obtain the Grüneisen EOS parameters C_o and S_1. The reference density is volume-fraction-averaged [see Eq. (3)].

3. Mixture Rule Based on Mass-Fraction Averages (Method 3)

Method B by Meyers [22] is the less rigorous of the two methods and calculates EOS material parameters based on mass-fraction averages. This method has been employed in the study of SICRs [6]. Although this method has no physical basis, it is much simpler compared method 1 and method 2. In the example given by Meyers [22], the Mie–Grüneisen EOS parameters C_o and S_1 and the mixture reference density $\bar{\rho}_o$ are given by

$$\bar{C}_o = \sum_p \phi_p C_{op}; \qquad \bar{S}_1 = \sum_p \phi_p S_{1p}; \qquad \bar{\rho}_o = \sum_p \phi_p \rho_{op} \tag{46}$$

Here, we calculate the mass averages for $\bar{C}_v$ and $\bar{\Gamma}$ using Eq. (42).

B. Fully-Dense-Mixture Equation-of-State Characterization

Method 1 and method 3 are compared using the constituent Mie–Grüneisen EOS parameters, with the exception of method 1, which requires Murnaghan EOS parameters. For the homobaric method, the pressure difference between using Mie–Grüneisen and adjusted Murnaghan EOS constituent parameters is less than 1% for the pressure range considered in this paper (see Fig. 3). We compare the two proposed EOS methods with methods 1–3 for the fully dense stoichiometric mixture of 2Al and Fe_2O_3 with and without 20 wt % Epon 828 in Fig. 3a, with the exception of method 2 in Fig. 3b (see the subsequent explanation).

1. Homobaric and Uniform-Strain Methods:

The uniform-strain method calculates higher pressures compared with the homobaric method in Fig. 3. The uniform-strain method provides higher pressures for the same relative volume change, because the material with the highest bulk modulus dominates the load-carrying capability of the mixture. This effect is exaggerated with the addition of Epon 828, because this constituent has a low bulk modulus and high volume fraction compared with the other constituents.

2. Method 1:

For both mixtures (with and without Epon 828) in Fig. 3, method 1 closely approximates the homobaric method up to $P = 10$ GPa. This agreement is not surprising, because the bulk modulus and its pressure derivative are volume-fraction-averaged in Eq. (39) at the $T = 298$ K isotherm.

Method 1 deviates from the homobaric method at higher-temperature isotherms for high-temperature and low-pressure conditions, as shown in Fig. 4. This illustrates a fundamental aspect of the homobaric method, in which the constant-volume thermal contribution to the pressure has nonphysical effects. Here, the homobaric assumption is invalid because the thermal pressure contribution in one of the constituents will be too high. Therefore, constituent pressures cannot be equilibrated without imposing either negative pressures or negative volume fractions, both of which are nonphysical. Therefore, we impose $P_p \geq 0$ and $\xi_p \geq 0$ for all constituents. The homobaric method approximates the uniform-strain method as $v \to v_o$, because the constituent pressures are not equal at the lower pressures in Fig. 4. Method 1 does not have the pressure and temperature limitations that are displayed for the homobaric method. However, method 1 is nonphysical because there cannot be any physical pressure equilibration between the constituents.

3. Method 2

This method is shown in Fig. 3a to predict lower pressures than the homobaric method; thus, results from method 2 are not bounded by the homobaric and uniform-strain methods. This method is an acceptable approximation for some alloys and compounds [22]. For the alloy mixture in this study, we see in Fig. 3a that method 2 does

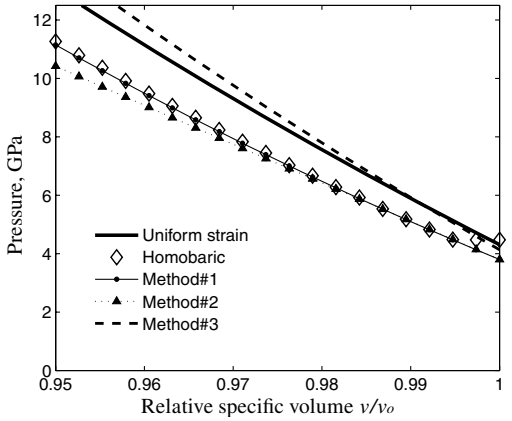

Fig. 4 $T = 1000$ K isotherm predicted by two-mixture EOS methods compared with the homobaric and uniform-strain methods for the fully dense stoichiometric mixture of 2Al and Fe_2O_3.

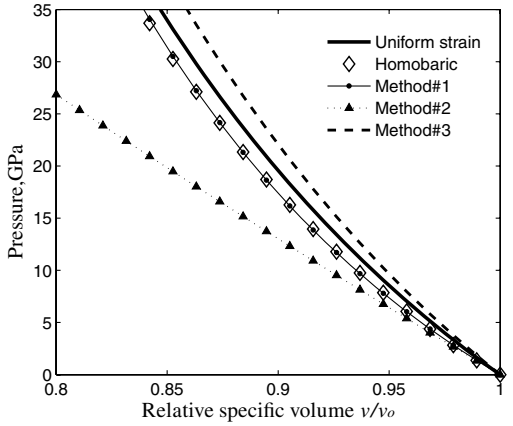

a) No Epon 828

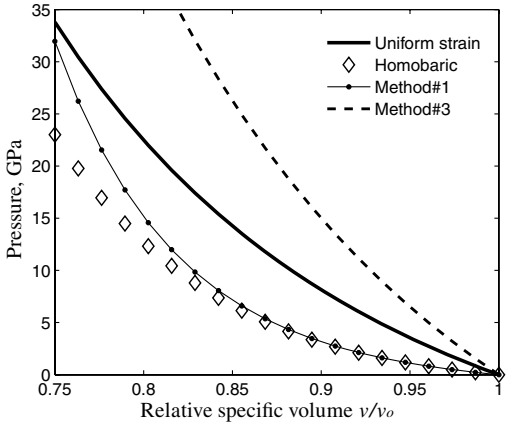

b) 20 wt% Epon 828

Fig. 3 $T = 298$ K isotherm predicted by three-mixture EOS methods compared with the homobaric and uniform-strain methods for the fully dense stoichiometric mixture of 2Al and Fe_2O_3 with and without 20 wt % Epon 828.

not reasonably approximate the case in which mechanical equilibrium is assumed for $P > 5$ GPa. Data could not be obtained from the MIXTURE program [33] for the 20 wt % Epon 828 case, due to its relatively low acoustic wave speed C_o.

4. *Method 3*

Mass averaging all of the Mie–Grüneisen EOS parameters leads to an overestimation of the mixture average density $\bar{\rho}$ for the stoichiometric 2Al and Fe_2O_3 mixture. The effects of this overestimation are indicated by elevated pressures that exceed the uniform-strain method, as seen in Fig. 3. Method 3 results are relatively close to the uniform-strain results when all mixture quantities are close to the same density (see Fig. 3a). However, when the 20 wt % Epon 828 is added, the pressure increases significantly due to the overestimation of $\bar{\rho}$.

C. Porous-Mixture Equation-of-State Characterization

We demonstrate the homobaric and uniform-strain methods applied to a porous stoichiometric mixture of 2Al and Fe_2O_3 with and without 20 wt % Epon 828 in Fig. 5 using Eqs. (35). Figures 5a and 5b compare the effect of adding Epon 828 with $n = 2$. Figures 5c and 5d show homobaric and uniform-strain methods with various orders n of α dependence on pressure with 20 wt % Epon 828. Here, we assume that $P^e = 250$ MPa and $P^s = 3$ GPa, based on experimental data for a mixture containing spherical Ni/Al particles [4] with the porosity $\alpha_o = 1.66$. As shown previously, the homobaric and uniform-strain methods show considerable differences when 20 wt % Epon 828 is included in the nonporous mixture. However, these pressure differences are much smaller for the porous mixture ($\alpha \geq 1$), because the mixture density $\bar{\rho}^d$ does not change significantly during pore collapse.

Homobaric and uniform-strain results are shown in Figs. 5c and 5d for distension-ratio pressure dependencies in the range of $n = 1$–4 [see Eq. (30)]. Higher values of n physically correspond to porous materials with lower strength. Parameter n may be adjusted to reflect the strength in porous mixtures with various morphologies such as flake and spherical powders [4].

D. Simulated Gas-Gun Experiment

Gas-gun and explosive loading experiments are simulated for the 2Al, Fe_2O_3, 50 wt % Epon 828, and $\alpha_o = 1.01$ material up to pressures of ~23 GPa [2]. Here, we simulate a copper driver plate, with 2 mm thickness, impacting the 2-mm-thick sample material. The material interface is given by the dashed vertical line close to $x = 2$ mm in Fig. 6a. The four plots include the pressure, particle velocity, temperature, and density along the x axis of the simulated copper (on the left) and the sample material (on the right). Included in Fig. 6a are the points used to calculate the pressure and particle velocity used for comparison with experimental data in Fig. 7.

Time history of the shock-front location is used to calculate the simulated shock velocity and is shown in Fig. 6b. The location is calculated from interpolating the particle velocity at a constant pressure that is approximately 50% of the shock pressure. Simulation results are shown with Courant–Friedrichs–Lewy (CFL) number CFL = 0.4, and 400 nodes along the x axis.

We solve the conservation equations using the MUSCL algorithm [34] and employ the Lax—Friedrichs flux. This method requires the calculation of the maximum eigenvalue that can be approximated by the sound speed C, which is given by

$$C^2 = \left(\frac{\partial P}{\partial \rho}\right)_e + \frac{P}{\rho^2}\left(\frac{\partial P}{\partial e}\right)_\rho \tag{47}$$

The maximum eigenvalue is approximated by

$$\lambda_i = \max_i\{C_i - \mathrm{v}_i, C_i, C_i + \mathrm{v}_i\} \tag{48}$$

for all i nodes in the sample material. The derivatives in Eq. (47) are approximated by first-order finite differences, because the homobaric and the uniform-strain methods are not differentiable.

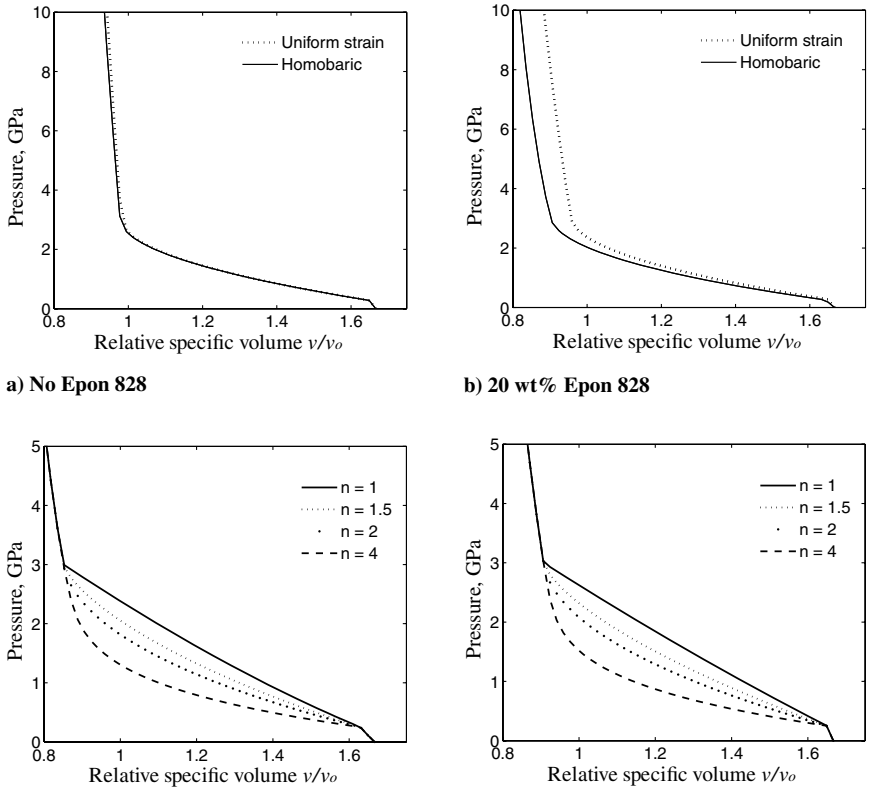

a) No Epon 828 **b) 20 wt% Epon 828**

c) Homobaric **d) Uniform strain**

Fig. 5 Simulation results with $P^e = 250$ MPa, and $P^s = 3$ GPa for the $T = 298$ K isotherm. The mixture is stoichiometric 2Al, Fe_2O_3, Epon 828, and $\alpha_o = 1.66$.

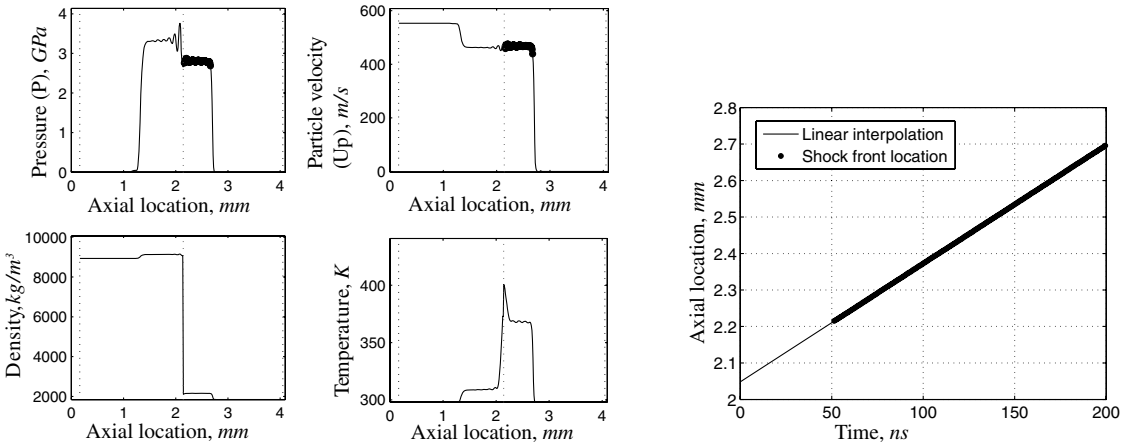

a) Simulation results at time $t = 200$ ns

b) Shock-front time history

Fig. 6 Simulation results with the copper flyer impact velocity $V_s = 553$ m/s for the stoichiometric mixture 2Al, Fe_2O_3, 50 wt % Epon 828, and $\alpha_o = 1.01$ with $n = 2$ and homobaric method. The data points used to interpolate P and Up are shown in the top two plots and appear as bold lines because $n_x = 400$ nodes are used.

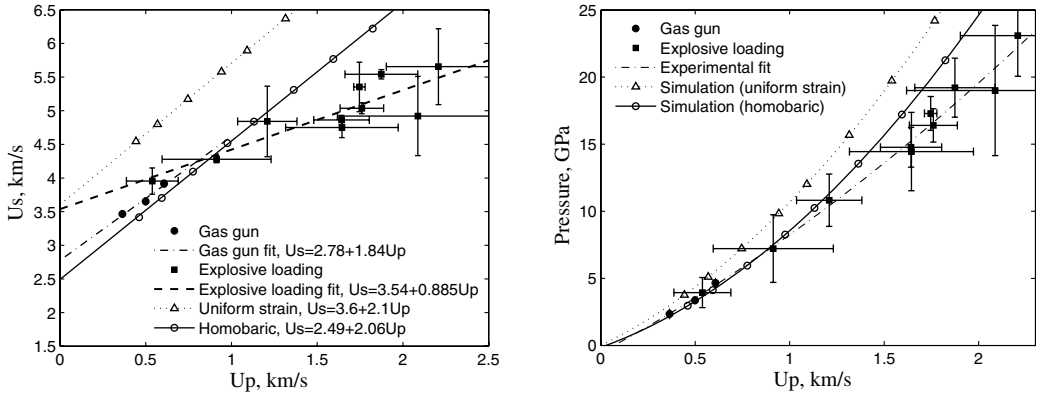

a) Shock velocity-particle velocity

b) Pressure-particle velocity

Fig. 7 Simulation results compared with experimental data for the stoichiometric mixture 2Al, Fe_2O_3, 50 wt % Epon 828, and $\alpha_o = 1.01$ with $n = 2$.

The material interface is tracked by the ghost-fluid method [35]. This method is nonconservative and overheating of the material can result, as pointed out by Glaister [36], which is observed in the temperature plot in Fig. 6a. Future work will employ conservative front tracking [35].

Figure 7 shows that the homobaric and uniform-strain methods bound the experimental data up to approximately $Up = 0.8$ km/s or $P = 6$ GPa. The pressure from the homobaric assumption is within the error bars of all but one experimental point ($Up = 607 \pm 0.004$ km/s) for pressures $P \leq 10$ GPa. For comparison, spatially resolved particle simulations resulted in $Us = 2.54 + 1.44Up$, which is within 7% error in low-pressure regimes and within 15% error in higher-pressure regimes [9].

V. Conclusions

The proposed porous-mixture EOS methods introduced in this paper are robust and represent homobaric and uniform-strain assumptions. These methods are useful in ESM studies and offer the following advantages over existing porous-mixture EOS methods:

1) Constituent EOS models are not required to have the same form and are not required to be easily inverted.

2) Any form of pore-collapse model may be employed. This permits the use of history-dependent models such as the Carroll–Holt model.

3) The mixture EOS is physically represented because material parameters are not averaged.

4) A weighted combination C_m of the two proposed methods may be used in continuum-scale codes such as finite element or finite volume codes.

The main disadvantage of the proposed methods is the increased number of iterations required. The extended VIR model [15] requires an estimated 4–8 iterations per time step, compared with the 10–20 iterations required in the proposed methods. Further computations are required to compute the approximate derivatives in Eq. (47).

The proposed algorithms are subject to limitations resulting from approximations made in constituent EOS models. For example, we observed that the homobaric assumption is invalid for low-pressure and high-temperature conditions. This limitation is not present if the constituent EOS model does not have a constant-volume thermal pressure contribution.

The case study results in Figs. 3 and 4 show that method 2 does not approximate the homobaric method nearly as well as method 1. Therefore, method 1 should be used instead of method 2 when mechanical equilibration is assumed in an alloy mixture. However, method 1 does not approximate the homobaric assumption at high pressures when the bulk moduli of constituents are considerably different. For example, agreement between method 1 and the homobaric model was observed for the 20 wt % Epon 828 case up to pressures near 10 GPa. Method 3 should be used with extreme caution as a crude approximation for materials with constituents that have similar densities.

The gas-gun simulations incorporate mixture strength in the stress tensor, which is not included in most of the previous continuum

SICR models considered in this study [1,6,15,16]. Simulation results show reasonable agreement with experimental data. Sources of uncertainty and errors due to discretization errors are given in a concurrent paper by the authors [38]. The homobaric and uniform-strain methods bound the experimental data up to approximately 5 GPa in Fig. 6. The homobaric method approximates the experimental data much better than the uniform-strain method. These results suggest that mechanical equilibrium is reached within the rise time of the shock.

Acknowledgments

This research was funded by the U.S. Air Force Office of Scientific Research Multidisciplinary University Research Initiative 1606U81 on Multifunctional Energetic Structural Materials at the Georgia Institute of Technology. We thank D. L. McDowell and R. A. Austin for their valuable input and suggestions and N. N. Thadhani and D. Eakins for helpful conversations on shock studies and for providing the MIXTURE code.

References

[1] Boslough, M. B., "A Thermochemical Model for Shock-Induced Reactions (Heat Detonations) in Solids," *Journal of Chemical Physics*, Vol. 92, No. 3, 1990, pp. 1839–1848. doi:10.1063/1.458066

[2] Jordan, J. L., Ferranti, L., Austin, R. A., Dick, R. D., Foley, J. R., Thadhani, N. N., McDowell, D. L., Benson, D. J., "Equation of State of Aluminum-Iron Oxide-Epoxy Composite," *Journal of Applied Physics*, Vol. 101, No. 9, 2007, Paper 093520.

[3] Xu, X., and Thadhani, N. N., "Investigation of Shock-Induced Reaction Behavior of As-Blended and Ball-Milled Ni + Ti Powder Mixtures Using Time-Resolved Stress Measurements," *Journal of Applied Physics*, Vol. 96, No. 4, 2004, pp. 2000–2009. doi:10.1063/1.1773380

[4] Eakins, D. E., and Thadhani, N. N., "Role of Constituent Configuration on Shock-Induced Reactions in a Ni + Al Powder Mixture," *2005 Materials Research Society Fall Meeting*, Materials Research Society, Warrendale, PA, 2006, pp. 191–196.

[5] Thadhani, N. N., Graham, R. A., Royal, T., Dunbar, E., Anderson, M. U., and Holman, G. T., "Shock-Induced Chemical Reactions in Titanium-Silicon Powder Mixtures of Different Morphologies: Time-Resolved Pressure Measurements and Materials Analysis," *Journal of Applied Physics*, Vol. 82, No. 3, 1997, pp. 1113–1128. doi:10.1063/1.365878

[6] Narayanan, V. N., "Non-Equilibrium Thermodynamics of Multifunctional Energetic Structural Materials," Ph.D. Thesis, Georgia Inst. of Technology, School of Aerospace Engineering, Atlanta, 2005.

[7] Reding, D. J., Lu, X., Narayanan, V. N., and Hanagud, S., "Constitutive Modeling of Multi-Functional Structural Energetic Materials: Plasticity Effects," 47th AIAA/ASME/ASCE/AHS/ASC Structures, Structural Dynamics, and Materials Conference, AIAA, Reston, VA, 2006, pp. 4387–4395.

[8] Austin, R. A., "Numerical Simulation of the Shock Compression of Microscale Reactive Particle Systems," M.S. Thesis, Georgia Inst. of Technology, Atlanta, 2005.

[9] Austin, R. A., McDowell, D. L., and Benson, D. J., "Numerical Simulation of Shock Wave Propagation in Spatially Resolved Particle Systems," *Modelling and Simulation in Materials Science and Engineering*, Vol. 14, No. 4, 2006, pp. 537–561. doi:10.1088/0965-0393/14/4/001

[10] Choi, H. J., Austin, R. A., Allen, J. K., McDowell, D. L., Mistree, F. M., and Benson, D. J., "An Approach for Robust Design of Reactive Powder Metal Mixtures Based on Nondeterministic Micro-Scale Shock Simulation," *Journal of Computer-Aided Materials Design*, Vol. 12, No. 1, 2005, pp. 57–85. doi:10.1007/s10820-005-1056-1

[11] Dremin, A. N., and Breusov, O. N., *Russian chemical reviews*, Vol. 37, No. 5, 1968, p. 392. doi:10.1070/RC1968v037n05ABEH001643

[12] Batsanov, S. S., Doronin, G. S., Kolchkov, S. V., Litvak, G. S., and Nigmatullina, V. M., "Synthesis Reactions Behind Shock Fronts," *Shock Waves*, Vol. 22, No. 6, 1986, p. 765.

[13] Graham, R. A., "High Pressure Explosive Processing of Ceramics," Trans Tech, Stafa-Zurich, Switzerland, July 1987.

[14] Song, I., and Thadhani, N. N., "Shock-Induced Chemical Reactions and Synthesis of Nickel Aluminides," *Metallurgical Transactions A (Physical Metallurgy and Materials Science)*, Vol. 23, No. 1, 1992, pp. 41–48. doi:10.1007/BF02660849

[15] Bennett, L. S., Horie, Y., and Hwang, M. M., "Constitutive Model of Shock-Induced Chemical Reactions in Inorganic Powder Mixtures," *Journal of Applied Physics*, Vol. 76, No. 6, 1994, pp. 3394–3402. doi:10.1063/1.357469

[16] Bennett, L. S., and Horie, Y., "Shock-Induced Inorganic Reactions and Condensed Phase Detonations," *Shock Waves*, Vol. 4, No. 3, 1994, pp. 127–136. doi:10.1007/BF01417428

[17] Do, I. P. H., and Benson, D. J., "Micromechanical Modeling of Shock-Induced Chemical Reactions in Heterogeneous Multimaterial Powder Mixtures," *International Journal of Plasticity*, Vol. 17, No. 4, 2001, pp. 641–668. doi:10.1016/S0749-6419(00)00065-6

[18] Lu, X., Narayanan, V. N., and Hanagud, S., "Shock Compression of Materials," *14th APS Topical Conference on Shock Compression of Condensed Matter*, Vol. 15, American Physical Society, College Park, MD, 2005.

[19] Do, I. P. H., and Benson, D. J., "Modeling of Shock-Induced Chemical Reactions," *International Journal of Computational Engineering Science*, Vol. 1, No. 1, 2000, pp. 61–79. doi:10.1142/S1465876300000057

[20] Thadhani, N. N., "Shock-Induced and Shock-Assisted Solid-State Chemical Reactions in Powder Mixtures," *Journal of Applied Physics*, Vol. 76, No. 4, 1994, pp. 2129–2138. doi:10.1063/1.357624

[21] McQueen, G., Marsh, S. P., Taylor, J. W., Fritz, J., and Carter, W. J., *High Velocity Impact Phenomena*, Academic Press, New York, 1970, p. 230.

[22] Meyers, M. A., *Dynamic Behavior of Materials*, Wiley, New York, 1994.

[23] Torunov, S. I., and Trofimov, V. S., "Detonation Hugoniots of Powdered Ti-C, Ti-B, Fe_2O_3–Al Mixtures with Gasifying Additives," *Chemical Physics Reports*, Vol. 17, No. 11, 1999, pp. 2167–2177.

[24] Herrmann, W., "Constitutive Equation for the Dynamic Compaction of Ductile Porous Materials," *Journal of Applied Physics*, Vol. 40, No. 6, 1968.

[25] Carroll, M. M., and Holt, A. C., "Static and Dynamic Pore Collapse Relations for Ductile Porous Materials," *Journal of Applied Physics*, Vol. 43, No. 4, 1972.

[26] Carroll, M. M., Kim, K. T., and Nesterenko, V. F., "The Effect of Temperature on Viscoplastic Pore Collapse," *Journal of Applied Physics*, Vol. 59, No. 6, 1986.

[27] Nesterenko, V. F., *High-Rate Deformation of Heterogeneous Materials*, Nauka, Novosibirsk, 1992 (in Russian).

[28] Nesterenko, V. F., *Dynamics of Heterogeneous Materials*, Springer–Verlag, New York, 2001.

[29] Rajagopal, K. R., and Tao, L., *Mechanics of Mixtures*, World Scientific, Singapore, 1995.

[30] Asay, J. R., and Shahinpoor, M., *High-Pressure Shock Compression of Solids*, Springer–Verlag, New York, 1993.

[31] Murnaghan, F. D., "Finite Deformations of an Elastic Solid," *American Journal of Mathematics*, Vol. 59, 1937, pp. 235–260. doi:10.2307/2371405

[32] Marsh, S. P., *LASL Shock Hugoniot Data*, Univ. of California Press, Los Angeles, 1980.

[33] Yoshida, M., "Program MIXTURE," New Mexico Inst. of Mining and Technology, Socorro, NM, 1986.

[34] Leer, V., "Towards the Ultimate Conservative Difference Scheme," *Journal of Computational Physics*, Vol. 32, No. 2, 1979, pp. 101–136.

[35] Glimm, J., Li, X., Liu, Y., Xu, Z., and Zhao, N., "Conservative Front Tracking and Level Set Algorithms," *Proceedings of the National Academy of Sciences*, Vol. 98, No. 25, 2001, pp. 14198–14201.

[36] Glaister, P., "An Approximate Linearised Riemann Solver for the Euler Equations for Real Gases," *Journal of Computational Physics*, Vol. 74, No. 2, 1988, pp. 382–408. doi:10.1016/0021-9991(88)90084-8

[37] *Aluminum Alloy Database* [online database], Knovel, New York, 2004, http://www.knovel.com/knovel2/Toc.jsp?BookID=844&VerticalID=0 [retrieved 17 Sept. 2007].

[38] Reding, D., and Hanagud, S., "Code Verification for Energetic Structural Material Simulations," *AIAA Journal* (to be published).

K. Shivakumar
Associate Editor